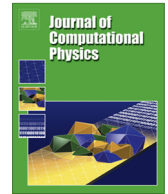




ELSEVIER

Contents lists available at SciVerse ScienceDirect

Journal of Computational Physics

journal homepage: www.elsevier.com/locate/jcp

Generalized Hamiltonian point vortex dynamics on arbitrary domains using the method of fundamental solutions



T.L. Ashbee*, J.G. Esler, N.R. McDonald

Department of Mathematics, University College London, Gower Street, London WC1E 6BT, UK

ARTICLE INFO

Article history:

Received 5 July 2012

Received in revised form 9 January 2013

Accepted 19 March 2013

Available online 6 April 2013

Keywords:

Method of fundamental solutions

Hamiltonian

Point vortices

ABSTRACT

A new algorithm (VOR-MFS) is presented for the solution of a generalized Hamiltonian model of point vortex dynamics in an arbitrary two-dimensional computational domain. The VOR-MFS algorithm utilizes the method of fundamental solutions (MFS) to obtain an approximation to the model Hamiltonian by solution of an appropriate boundary value problem. Unlike standard point vortex methods, VOR-MFS requires knowledge only of the free-space (\mathbb{R}^2) Green's function for the problem as opposed to the domain-adapted Green's function, permitting solution of a much wider range of problems. VOR-MFS is first validated against a vortex image model for the case of (2D Euler) multiple vortex motion in both circular and 'Neumann-oval' shaped domains. It is then demonstrated that VOR-MFS can solve for quasi-geostrophic shallow water point vortex motion in the same domains. The exponential convergence of the MFS method is shown to lead to good conservation properties for each of the solutions presented.

© 2013 Elsevier Inc. All rights reserved.

1. Introduction

The point vortex model of hydrodynamics is an important canonical problem with relevance to fluid turbulence, plasma physics, statistical mechanics and dynamical systems theory. Newton [32] gives a thorough review of recent research and some open problems (see also [29,38]). For the motion of N vortices in a simply connected domain $\mathcal{D} \subset \mathbb{R}^2$, each with circulation Γ_i ($i = 1, \dots, N$) the equations of motion are Hamiltonian,

$$\Gamma_i \dot{\mathbf{x}}_i = -\frac{\partial H}{\partial \mathbf{y}_i}, \quad \Gamma_i \dot{\mathbf{y}}_i = \frac{\partial H}{\partial \mathbf{x}_i}, \quad i = 1, \dots, N. \quad (1)$$

The system (1) is unusual only in that the scaled vortex coordinates $|\Gamma_i|^{1/2} \mathbf{x}_i$, where $\mathbf{x}_i = (x_i, y_i)^T$, take the role of canonical phase space coordinates.

In the most general formulation (e.g. [26]), the Hamiltonian can be written

$$H(\mathbf{x}_1, \dots, \mathbf{x}_N) = -\sum_{i=1}^N \sum_{j=i+1}^N \Gamma_i \Gamma_j G(\mathbf{x}_i, \mathbf{x}_j) - \frac{1}{2} \sum_{i=1}^N \Gamma_i^2 g(\mathbf{x}_i, \mathbf{x}_i) \quad (2)$$

and is a conserved quantity. The function $G(\mathbf{x}, \mathbf{x}')$ is the Green's function of the first kind for the domain \mathcal{D} , defined by

$$\mathcal{L}G(\mathbf{x}, \mathbf{x}') = \delta(\mathbf{x} - \mathbf{x}') \quad \mathbf{x}, \mathbf{x}' \in \mathcal{D}, \quad (3a)$$

* Corresponding author. Tel.: +44 07590255273.

E-mail address: ashbee@math.ucl.ac.uk (T.L. Ashbee).

$$G(\mathbf{x}, \mathbf{x}') = 0. \quad \mathbf{x} \in \partial\mathcal{D}. \quad (3b)$$

The linear elliptic operator \mathcal{L} , which acts on the \mathbf{x} variable only, is in most formulations of the problem taken to be the Laplacian ($\mathcal{L} \equiv \nabla^2$), and the result is the point vortex dynamical system of the 2D Euler equations. However, as discussed below, other choices of \mathcal{L} result in alternative point vortex dynamics with relevance to various problems in geophysical fluid dynamics. Here, we define *generalized point vortex dynamics* to refer to the dynamical system defined by (1)–(3) for any choice of invertible and self-adjoint linear elliptic operator \mathcal{L} . (Self-adjointness of \mathcal{L} guarantees the symmetry $G(\mathbf{x}, \mathbf{x}') = G(\mathbf{x}', \mathbf{x})$ required below.) The remaining function $g(\mathbf{x}, \mathbf{x}')$ appearing in (2), which we shall term the residual Green's function (or the Robin function when \mathcal{L} is the Laplacian operator), is defined by $g(\mathbf{x}, \mathbf{x}') = G(\mathbf{x}, \mathbf{x}') - G_0(\mathbf{x}, \mathbf{x}')$ where G_0 is the corresponding free-space (\mathbb{R}^2) Green's function satisfying

$$\mathcal{L}G_0(\mathbf{x}, \mathbf{x}') = \delta(\mathbf{x} - \mathbf{x}') \quad \mathbf{x}, \mathbf{x}' \in \mathbb{R}^2, \quad (4a)$$

$$|\nabla G_0(\mathbf{x}, \mathbf{x}')| \rightarrow 0 \quad |\mathbf{x} - \mathbf{x}'| \rightarrow \infty. \quad (4b)$$

A requirement in all that follows is that, given a specific operator \mathcal{L} , an explicit expression (or means of numerical evaluation) is available for the corresponding free space Green's function $G_0(\mathbf{x}, \mathbf{x}')$.

Numerical solution of the system (1) has understandably focused on the 2D Euler system, for which

$$\mathcal{L} \equiv \nabla^2, \quad G_0(\mathbf{x}, \mathbf{x}') = \frac{1}{2\pi} \log(|\mathbf{x} - \mathbf{x}'|).$$

Although most early calculations (e.g. [35]) have focussed on circular or periodic domains for which explicit expressions for G (and thus g) are available via the method of images, it has been long known [27] that the 2D Euler point vortex system can be solved in any simply-connected domain \mathcal{D} using the conformal map to the unit circle. The method exploits the so-called Routh rule to make suitable modifications to the Hamiltonian H (see for example p. 130 of [32]). Recent work [7] has extended these results to multiply-connected domains.

For systems governed by operators other than the Laplacian, however, the method of images is typically restricted to domains with straight boundaries, and the Routh rule does not apply. Consequently, our aim here is to formulate a new algorithm that solves (1) for a general linear operator \mathcal{L} . In the case of the 2D Euler system the new algorithm has the advantage of allowing solutions in domains for which an explicit conformal map is not known.

A first important example of point vortex dynamics governed by an operator other than the Laplacian is the so-called 'quasi-geostrophic shallow water' (QGSW) system [34], for which \mathcal{L} is a modified Helmholtz operator

$$\mathcal{L} \equiv \nabla^2 - \lambda^2, \quad G_0(\mathbf{x}, \mathbf{x}') = -\frac{1}{2\pi} K_0(\lambda|\mathbf{x} - \mathbf{x}'|), \quad (5)$$

where $K_0(\cdot)$ is a modified Bessel function of the second kind. Here λ^{-1} has the dimension of length and is known as the Rossby deformation radius. The system (5) is relevant to the dynamics of ocean vortices where typically λ^{-1} is taken to be of the order of 10–50 km. QGSW dynamics differs from that of 2D Euler in that the dynamical influence of QGSW vortices decays rapidly on lengthscales $\sim \lambda^{-1}$, localizing the dynamics.

A second example is the 'surface quasi-geostrophic' (SQG) system [17], for which

$$\mathcal{L} \equiv -(-\nabla^2)^{1/2}, \quad G_0(\mathbf{x}, \mathbf{x}') = -\frac{1}{2\pi} (|\mathbf{x} - \mathbf{x}'|)^{-1}.$$

The SQG system describes the motion induced by surface concentrated potential vorticity anomalies in the ocean or atmosphere, or equivalently, surface potential buoyancy anomalies (ocean) or potential temperature anomalies (atmosphere) at the planetary surface or tropopause [19]. The singularity associated with an SQG vortex is a simple pole rather than a logarithmic singularity, and the result is a dynamics that is much more active on small scales [17]. The turbulent cascade in the SQG model is also thought relevant to three-dimensional turbulence in the Euler equations [6].

Several different numerical algorithms have been employed to solve (1) in the 2D Euler case. Two major limitations of such algorithms, that we do not try to resolve here, are firstly that $O(N^2)$ evaluations of the partial derivatives of G and g are required at each timestep (though improvements could be made using approximate methods such as [16]) and secondly that variable time-stepping is necessary in order to resolve trajectories on the intermittent occasions when vortices pass close together. Bühler [3] describes these issues in the context of a standard adaptive algorithm for N vortices in a circular domain. It is difficult to avoid the $O(N^2)$ costs without resorting to approximate methods (e.g. [5]), and efforts at calculations for large N ($N \approx 7000$ at the time of writing) have instead been focussed on supercomputing efforts using specialized hardware [42].

One important feature that must be respected by any such algorithm is the invariance of the Hamiltonian H . Symplectic methods [36,43] have been shown to have greatly improved conservation properties at fixed time-step. However this technique also scales $O(N^2)$, and can have poor stability properties when used with a variable time step (which is necessary for large N simulations), though an alternative adaptive scheme is suggested in [30]. Two aspects of the symplectic method that have yet to be explored are its effectiveness in bounded domains and for large N simulations. Extensive transformations of

the Hamiltonian would also be required in order for it to be used with a symplectic integrator. Therefore, to keep the presentation simple, we use as our starting point a basic (but adaptive) algorithm in the spirit of that suggested by Bühler [3].

The new algorithm (VOR-MFS hereafter) is designed to solve the generalized point vortex problems detailed above by exploiting the method of fundamental solutions (MFS hereafter), see [12,14] for detailed overviews. The idea of the MFS is to approximate the dynamical influence of the domain boundary at each vortex location using a linear combination of free-space (G_0) Green's function solutions (the fundamental solutions). The locations of the singularities associated with the fundamental solutions lie outside \mathcal{D} on a set of points known as the MFS charge points, and the weights attached to each charge are chosen to satisfy the Dirichlet boundary condition (3b) on a discrete set of boundary points on $\partial\mathcal{D}$. The method is particularly simple to implement and has excellent convergence properties that will be discussed below. Apart from the recent work of Wu et al. [41], who apply MFS to the relatively straightforward problem of the motion of a single 2D Euler vortex outside an elliptical cylinder, to our knowledge VOR-MFS represents the first attempt to exploit the MFS in this context.

The article is structured as follows: Section 2 introduces the new algorithm VOR-MFS and reviews the relevant aspects of the MFS method. A protocol for choosing numerical parameters to obtain numerical solutions to a pre-determined accuracy is described. Section 3 describes a number of test-cases demonstrating the robustness of the new algorithm. Finally, in Section 4 conclusions are presented along with possible directions for future research.

2. The VOR-MFS algorithm

2.1. The adaptive timestepping algorithm

The new algorithm VOR-MFS to be described below is built upon a standard adaptive time-stepping algorithm designed to solve (1). The adaptive time-stepping component is deliberately chosen to be as simple as possible in order not to detract from the new aspects described below, it is essentially that of Bühler [3], and proceeds by targeting solutions of (1) over intervals of length Δt . To advance the solution from the current time $t = t_n$ ($t_n = n\Delta t$), the equations of motion are solved repeatedly over the time interval $[t_n, t_n + \Delta t]$, by subdividing the interval into 2^m substeps ($m = 1, 2, 3, \dots$), and integrating over the substeps using an explicit fourth-order Runge–Kutta method. If the solution at $t_n + \Delta t$ obtained using 2^m substeps is denoted $\{\mathbf{x}_1^{(m)}, \dots, \mathbf{x}_N^{(m)}\}$, then the stopping criterion for the interval is defined to be

$$\frac{1}{N} \sum_{i=1}^N |\mathbf{x}_i^{(m)} - \mathbf{x}_i^{(m-1)}| < \delta, \tag{6}$$

i.e. the mean absolute vortex positions must converge to be less than δ . The numerical parameter δ controls the accuracy of the VOR-MFS algorithm, and will be referred to as the *tolerance parameter* below.

The stopping criterion will be first met for some $m = m_*$, and the algorithm then moves onto the next time interval $[t_{n+1}, t_{n+1} + \Delta t]$. In practice, when many vortices are present, the number of substeps required (i.e. 2^{m_*}), varies quite considerably. This is due to intermittent episodes during which vortices pass close together, and it is the resolution of these episodes which explains the need for adaptivity.

If an exact expression for the Hamiltonian H is available, the equations of motion can be integrated directly using the above method. The new algorithm VOR-MFS extends the above algorithm to situations where no such explicit expression is available.

2.2. Use of the method of fundamental solutions

A standard problem for which the MFS has been designed is the boundary value problem

$$\mathcal{L}\phi(\mathbf{x}) = 0 \quad \mathbf{x} \in \mathcal{D}, \tag{7a}$$

$$\phi(\mathbf{x}) = b(\mathbf{x}) \quad \mathbf{x} \in \partial\mathcal{D}, \tag{7b}$$

where $b(\mathbf{x})$ is specified on the domain boundary $\partial\mathcal{D}$.

The MFS exploits the fact that the free-space Green's function $G_0(\mathbf{x}, \mathbf{x}')$ (see Eq. (4a) above) satisfies $\mathcal{L}G_0(\mathbf{x}, \mathbf{x}') = 0$ everywhere in \mathcal{D} , provided that \mathbf{x}' lies outside \mathcal{D} . The key idea in the MFS is simply to approximate $\phi(\mathbf{x})$ using a linear combination $\phi_M(\mathbf{x})$ of M free-space Green's functions, centered on a fixed set of points $\{\mathbf{y}_1, \dots, \mathbf{y}_M\}$ located outside \mathcal{D} , known as the MFS charge points. In summary,

$$\phi_M(\mathbf{x}) = \sum_{k=1}^M \alpha_k G_0(\mathbf{x}, \mathbf{y}_k), \quad \mathbf{x} \in \mathcal{D}, \quad \mathbf{y}_k \notin \mathcal{D}, \tag{8}$$

where the $\{\alpha_k\}$ are a set of weights. The weights are determined by enforcing the boundary condition (7b) on a discrete set of points $\{\mathbf{x}_j^B\}$ located on $\partial\mathcal{D}$. (For the purposes of the discussion here, and for the VOR-MFS algorithm, it will be assumed that there are M such boundary points. In some circumstances it has been shown [39] that the use of a number greater than M can be advantageous.) The result is a M -dimensional linear system in the $\{\alpha_k\}$, i.e.

$$\mathbf{G}\boldsymbol{\alpha} = \mathbf{b}, \tag{9}$$

where the $M \times M$ matrix \mathbf{G} has components $\{G_0(\mathbf{x}_j^B, \mathbf{y}_k)\}$, the vector $\boldsymbol{\alpha}$ components $\{\alpha_k\}$ and the vector \mathbf{b} components $\{b(\mathbf{x}_j^B)\}$. Eq. (9) can be solved for the $\{\alpha_k\}$ using a standard algorithm (e.g. the Gaussian elimination routine supplied by the software package MATLAB). Note that the matrix \mathbf{G} need only be inverted once at the beginning of a simulation. A possible limitation with the MFS is that the linear system (9) can be ill-conditioned [22,23]. However there is evidence in the literature [2,13–15] that apparent ill-conditioning of the MFS-problem presents minimal practical problems for the exponential convergence of the solution in Helmholtz and Laplacian boundary value problems. The essence of the problem is that the object of interest in the MFS problem is the convergence of the quantity ϕ_M in (8) and not the convergence of the individual charge weights $\{\boldsymbol{\alpha}\}$ themselves. Kitagawa [22,23] has studied precisely this problem and has found that errors are magnified by a quantity $O(M)$ relative to the error when no ill-conditioning is present (which of course decreases exponentially in M). The essential point is that those degrees of freedom in $\{\boldsymbol{\alpha}\}$ that cannot be determined accurately (due to ill-conditioning of the linear problem (9)) are precisely those that do not contribute significantly to ϕ_M .

In practice the ill-conditioning is not typically found to affect the accuracy of the MFS solutions. However, for a particular set-up, it is recommended that the singular values of the matrix \mathbf{G} are examined (i.e. prior to commencing a VOR-MFS integration).

A detailed discussion of the convergence and stability of the MFS is given in [12,14] and references therein. For the illustrative problems of Laplace’s equation and the Helmholtz equation in the unit cylinder, it has been shown [1,20,21] that if the MFS charge points are situated at radius $R > 1$ then the solution converges exponentially with M

$$\max_{\mathbf{x} \in \mathcal{D}} |\phi(\mathbf{x}) - \phi_M(\mathbf{x})| = O(R^{-M})$$

provided that $R < \sqrt{\rho}$, where ρ is the radius of first singularity of the analytic continuation of the solution in the complex plane. For other geometries, exponential convergence can also be attained, but the situation can be more complicated [1].

To use the MFS to solve (1) in the absence of an explicit expression for the domain Green’s function $G(\mathbf{x}, \mathbf{x}')$, note that by subtracting (4a) from (3a) the following equation for the residual Green’s function $g(\mathbf{x}, \mathbf{x}')$ is obtained

$$\mathcal{L}g(\mathbf{x}, \mathbf{x}') = 0 \quad \mathbf{x}, \mathbf{x}' \in \mathcal{D}, \tag{10a}$$

$$g(\mathbf{x}, \mathbf{x}') = -G_0(\mathbf{x}, \mathbf{x}'). \quad \mathbf{x} \in \partial\mathcal{D}. \tag{10b}$$

Since the free-space Green’s function G_0 is known everywhere, Eq. (10a) is exactly of the form (7a) (for given \mathbf{x}') and consequently a standard MFS routine can be straightforwardly applied to solve for an MFS approximation $g_M(\mathbf{x}, \mathbf{x}')$ to the residual Green’s function, thus obtaining a corresponding approximation to $G(\mathbf{x}, \mathbf{x}')$.

The above approach can be extended to solve for an MFS approximation to the N -vortex Hamiltonian H (denoted H_M) by linearity, with still just a single MFS calculation required. The relevant boundary value problem is

$$\mathcal{L}\phi(\mathbf{x}) = 0 \quad \mathbf{x} \in \mathcal{D}, \tag{11a}$$

$$\phi(\mathbf{x}) = -\sum_{j=1}^N \Gamma_j G_0(\mathbf{x}, \mathbf{x}_j) \quad \mathbf{x} \in \partial\mathcal{D}, \tag{11b}$$

which from (10a) has exact solution

$$\phi(\mathbf{x}) = \sum_{j=1}^N \Gamma_j g(\mathbf{x}, \mathbf{x}_j).$$

It is straightforward to verify that an alternative expression for the Hamiltonian (2) is

$$H = -\sum_{i=1}^N \sum_{j=i+1}^N \Gamma_i \Gamma_j G_0(\mathbf{x}_i, \mathbf{x}_j) - \frac{1}{2} \sum_{i=1}^N \Gamma_i \phi(\mathbf{x}_i).$$

A standard application of the MFS provides an approximate expression ϕ_M for ϕ from (8), which allows us to define an MFS Hamiltonian

$$H_M(\mathbf{x}_1, \dots, \mathbf{x}_N) = -\sum_{i=1}^N \sum_{j=i+1}^N \Gamma_i \Gamma_j G_0(\mathbf{x}_i, \mathbf{x}_j) - \frac{1}{2} \sum_{i=1}^N \sum_{k=1}^M \Gamma_i \alpha_k G_0(\mathbf{x}_i, \mathbf{y}_k), \tag{12}$$

where the $\{\alpha_k\}$ are the MFS weights obtained from the MFS solution of (11a).

The partial derivatives of the MFS Hamiltonian can be evaluated directly from (12) to integrate (1), bypassing the need for an explicit expression for $G(\mathbf{x}, \mathbf{x}')$. Because H is a conserved quantity, a key test of the algorithm is conservation of H_M . This will be investigated below.

2.3. The use of pseudo-images

One factor that strongly influences the accuracy and convergence of the MFS algorithm is the smoothness of the boundary function $b(\mathbf{x})$ in (7b) [1]. In particular, if $b(\mathbf{x})$ varies on spatial scales comparable to the spacing between MFS charge points (i.e. has significant spectral power at wavenumbers $\sim M|\mathcal{D}|^{-1/2}$ or greater, where $|\mathcal{D}|$ is the domain area), then the MFS solution will be unable to resolve the associated fine scale structure in $b(\mathbf{x})$ near the domain boundary. Ref. [1] recommend up to 10 MFS charge points per wavelength for the case where $b(\mathbf{x})$ consists of a single Fourier wavenumber, to obtain solutions close to machine precision.

For the specific MFS boundary value problem (11a) solved in VOR-MFS the boundary function appearing on the r.h.s. remains smooth everywhere on $\partial\mathcal{D}$, except where a vortex approaches the boundary. A vortex \mathbf{x}_j located a distance ε from the domain boundary will induce a spectral peak in the boundary data at wavenumbers $\sim \varepsilon^{-1}$. If vortices are to move freely in the domain, close encounters with the boundary are inevitable, and the MFS method will fail whenever $\varepsilon^{-1} \gtrsim M|\mathcal{D}|^{-1/2}$ for the reason outlined above.

There turns out to be a simple solution of the above problem. If an additional ‘pseudo-image’ vortex of opposite sign is placed at a suitable point \mathbf{x}_j^* on the opposite side of the boundary $\partial\mathcal{D}$ to the ‘problem’ vortex \mathbf{x}_j , then the spectral peak in the boundary data is smoothed and the MFS solution will retain its accuracy. There is considerable flexibility in the precise choice of \mathbf{x}_j^* , because all that is required is that as \mathbf{x}_j approaches the domain boundary ($\varepsilon \rightarrow 0$) is that $\mathbf{x}_j^* \rightarrow \tilde{\mathbf{x}}_j$, (more precisely it is required that $\lim_{\varepsilon \rightarrow 0} |\mathbf{x}_j^* - \tilde{\mathbf{x}}_j|/\varepsilon = 0$), where $\tilde{\mathbf{x}}_j$ is the reflected point generated by the nearest point on $\partial\mathcal{D}$ to \mathbf{x}_j , as illustrated in Fig. 1(a). For example, the locations of the exact 2D Euler images in the unit circle $\mathbf{x}_j^* = \mathbf{x}_j/|\mathbf{x}_j|^2$ are easily shown to converge towards the reflection point $\tilde{\mathbf{x}}_j$, as required. It is to be emphasized that the pseudo-image is not (necessarily) an exact image of the vortex at \mathbf{x}_j , merely an approximate image that becomes exact in the limit $\varepsilon \rightarrow 0$.

One possible choice for the pseudo-image position \mathbf{x}_j^* is the boundary reflection point $\tilde{\mathbf{x}}_j$ itself. However, in some relatively simple geometries $\tilde{\mathbf{x}}_j$ is a discontinuous function of \mathbf{x}_j , which can lead to computationally undesirable jumps in the pseudo-image position as \mathbf{x}_j evolves in time. In the examples below, knowledge of an explicit conformal map to the unit circle is exploited to choose \mathbf{x}_j^* , see below for details. Alternative methods of selecting \mathbf{x}_j^* are no doubt possible. In practice pseudo-images are introduced smoothly as a vortex approaches the boundary. For example, in a circular domain with unit radius the pseudo-image strength is set by the function

$$\hat{\Gamma}_j = -\Gamma_j \begin{cases} 0, & 0 \leq |\mathbf{x}_j| \leq R_1, \\ \left(\frac{|\mathbf{x}_j| - R_1}{R_2 - R_1}\right)^2, & R_1 < |\mathbf{x}_j| \leq R_2, \\ 1, & R_2 < |\mathbf{x}_j| \leq 1. \end{cases} \quad (13)$$

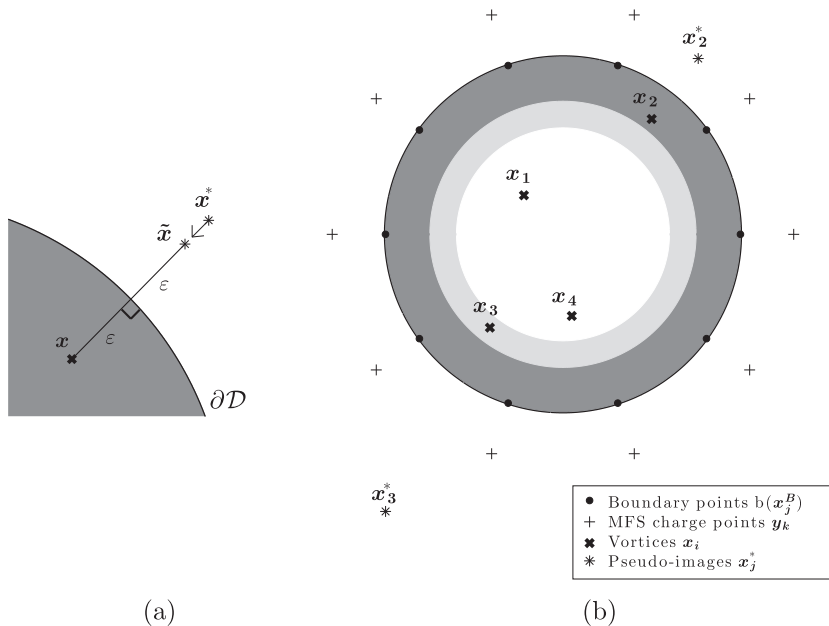


Fig. 1. (a) Schematic illustrating the boundary reflection point $\tilde{\mathbf{x}}$ and a possible pseudo-image location \mathbf{x}^* associated with a vortex at \mathbf{x} . (b) Schematic illustrating a typical configuration of vortices and pseudo-images in the unit circle domain (with $N = 4$). For vortices in central white region $|\mathbf{x}_j| \leq R_1$ no pseudo-images are used. In the dark grey region $|\mathbf{x}_j| > R_2$ a full strength pseudo-image is present, whereas in the light grey region $R_1 < |\mathbf{x}_j| \leq R_2$ the strength of the pseudo-image is gradually increased as the vortex moves closer to the boundary.

In domains that are conformal to the unit circle a similar approach can be taken (see below). Fig. 1(b) illustrates schematically the three regions in (13), some vortices and pseudo-images, and the MFS charge points.

In the case where there are $P \leq N$ pseudo-images, the MFS Hamiltonian is

$$H_M(\mathbf{x}_1, \dots, \mathbf{x}_N) = -\sum_{i=1}^N \sum_{j=i+1}^N \Gamma_i \Gamma_j G_0(\mathbf{x}_i, \mathbf{x}_j) - \frac{1}{2} \sum_{i=1}^N \sum_{k=1}^M \Gamma_i \tilde{\alpha}_k G_0(\mathbf{x}_i, \mathbf{y}_k) - \frac{1}{2} \sum_{i=1}^N \sum_{j=1}^P \Gamma_i \hat{\Gamma}_j(\mathbf{x}_j) G_0(\mathbf{x}_i, \mathbf{x}_j^*), \tag{14}$$

where $\{\tilde{\alpha}_k\}$ are the weights obtained from the MFS solution of

$$\mathcal{L}\phi(\mathbf{x}) = 0 \quad \mathbf{x} \in \mathcal{D}, \tag{15a}$$

$$\phi(\mathbf{x}) = -\sum_{j=1}^N \Gamma_j G_0(\mathbf{x}, \mathbf{x}_j) - \sum_{j=1}^P \hat{\Gamma}_j G_0(\mathbf{x}, \mathbf{x}_j^*) \quad \mathbf{x} \in \partial\mathcal{D}. \tag{15b}$$

Placement of pseudo-images can become complicated (or even impossible) when parts of the domain are very thin (e.g. a flat plate or protrusion), such as in [33]. Further, the convergence properties of the algorithm in this context will also be severely reduced, as will be noted in the next section.

2.4. Selection of the location and number of MFS charge points in VOR-MFS

The optimal positioning of the MFS charge points $\{\mathbf{y}_k\}$ and boundary points $\{\mathbf{x}_k^B\}$ is a topic that has received considerable attention in the literature (see e.g. [1]). The optimal distance of the curve on which the charge points are situated from the domain boundary $\partial\mathcal{D}$ depends in general upon the nature of the boundary data $b(\mathbf{x})$ in Eq. (7b), as well as the curvature of the domain boundary $\partial\mathcal{D}$. A detailed analysis of the optimal location of $\{\mathbf{y}_k\}$ specific to the VOR-MFS problem awaits a future study. The spacing of the charge points $\{\mathbf{y}_k\}$ along the chosen curve must reflect the curvature of $\partial\mathcal{D}$ itself. Unsurprisingly, the best results are obtained if the charge points are concentrated near regions of high curvature.

As mentioned in Section 2.3, vortex motion around thin obstacles will lead to severely reduced convergence properties. When the spacing between charge points exceeds the thickness of the obstacle, VOR-MFS is likely to have the more modest quadratic convergence properties of a boundary integral method such as [33]. VOR-MFS is evidently not suited to this specific problem and as such the focus of the paper will be on domains with no thin sections.

Good results have been obtained in the unit circle domain by placing the charge points uniformly at radius $R = 1.1$. In other domains, a conformal map from the unit circle domain to \mathcal{D} can be used to determine the positions of $\{\mathbf{y}_k\}$ based on a simple distribution around the circle. The boundary points $\{\mathbf{x}_k^B\}$ are placed uniformly around the circle $R = 1$ and then mapped onto $\partial\mathcal{D}$. The use of the conformal map, where available, ensures that the charge points are concentrated in the desired regions [1], however heuristic methods may well work where no conformal map is available.

Once an optimal curve for the MFS charge points $\{\mathbf{y}_k\}$ has been chosen, a crucial issue in optimizing the performance of VOR-MFS is the choice of the number M of charge points. The basic adaptive time-stepping algorithm described in Section 2.1 above requires convergence of the mean vortex position to within a tolerance δ (see Eq. 6) over a time interval Δt . For given δ , the optimal choice of M will be $M_*(\delta)$, defined to be the minimum value of M for which the accumulated error due to the MFS approximation over the interval $[t_n, t_n + \Delta t]$ is less than $\epsilon\delta$. Here $\epsilon < 1$ is a constant chosen to ensure that MFS errors at $M = M_*(\delta)$ remain sufficiently small compared with the errors associated with the adaptive time-stepping scheme itself.

For a specific set-up, the value of $M_*(\delta)$ can be estimated prior to a dynamical integration by the following procedure. A set of random vortex positions $\{\mathbf{x}_i\}$ is first generated. The mean error in velocity \mathbf{u}_i at the vortex locations due to the MFS is then defined to be

$$E(M) = \frac{1}{N} \sum_{i=1}^N \left| \mathbf{u}_i^{(M)} - \mathbf{u}_i \right|, \tag{16}$$

where $\mathbf{u}_i^{(M)}$ is the MFS estimate of \mathbf{u}_i . Next, the fact that MFS solutions converge exponentially in M , is exploited to write the following estimate for $E(M)$

$$E(M) \approx \frac{1}{N} \sum_{i=1}^N \left| \mathbf{u}_i^{(M)} - \mathbf{u}_i^{(M_{max})} \right| = Ae^{-\alpha M}, \tag{17}$$

where M_{max} is the maximum number of points for which the MFS problem can be conveniently solved. Estimates for the real constants A and α are found by using (17) to calculate $E(M)$ for several values of $M < M_{max}$ and making a least squares fit to $\log E(M)$. The values of A and α thus obtained are specific to the problem being solved, and also depend to a certain extent on numerical choices such as the locations of $\{\mathbf{y}_k\}$, the values of R_1, R_2 etc. In practice a number of realizations of $\{\mathbf{x}_i\}$ are tested and the ‘worst case’ values of A and α are used below.

Provided Δt is sufficiently small, the MFS error in mean vortex position over the time interval Δt can be estimated to be $E(M)\Delta t$. The requirement that

$$E(M)\Delta t \leq \epsilon\delta \tag{18}$$

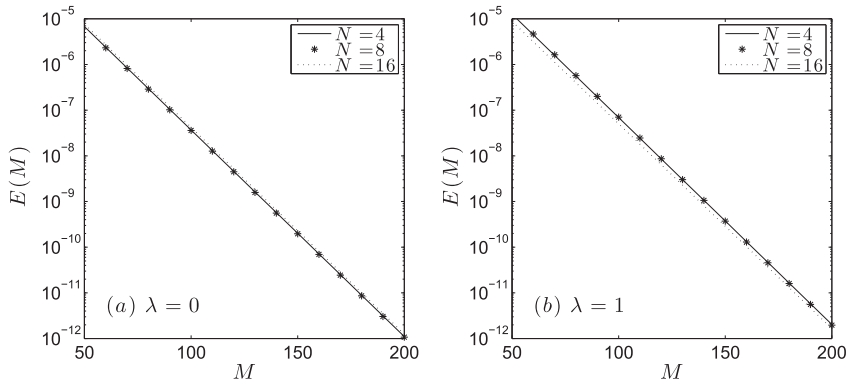


Fig. 2. MFS mean velocity error $E(M)$ for (a) the 2D Euler system and (b) the QGSW system, with $N = 4$, $N = 8$ and $N = 16$ in the unit circle. The results are calculated from the ‘worst’ case outcome of ten uniformly distributed random configurations of the N vortices.

is sufficient for the estimated MFS error to be less than the time-stepping error (by a factor ϵ). Our estimate of $M_*(\delta)$ is defined by equality in the above relation, and using (17) is found to be

$$M_*(\delta) = -\frac{1}{\alpha} \log \left(\frac{\epsilon \delta}{A \Delta t} \right). \quad (19)$$

The important point evident from (19) is that $M_*(\delta)$ has logarithmic dependence on δ . Consequently, provided the constant α is not too small, appropriately small values of δ can be targeted at little additional cost in terms of MFS charge points. A conservative choice of $\epsilon = 10^{-3}$ is made in all integrations described below, to ensure that time-stepping errors dominate over MFS errors.

The dependence of $E(M)$ on N is shown in Fig. 2 for the neutral (equal numbers of positive and negative vortices) in (a) the 2D Euler system ($\lambda = 0$) and (b) the QGSW system ($\lambda = 1$), with $N = 4$, $N = 8$ and $N = 16$ in a unit circle. Charge points are placed at a radius of 1.1, $\Delta t = 0.1$ and $\Gamma_i = \pm 1$. Ten realizations of the vortex positions are used for each calculation. It is clear from Fig. 2 that the mean error $E(M)$ in the vortex velocities depends at most weakly on N and on λ .

2.5. Computational cost of VOR-MFS

The structure of the VOR-MFS Hamiltonian (14) makes possible simple scaling estimates for the computational costs of VOR-MFS in comparison with an explicit numerical scheme designed to solve the same problem. How, for example, does the VOR-MFS algorithm scale with vortex number N and the accuracy controlling (tolerance) parameter δ ?

First note that a single evaluation of the linear problem (9) requires $M_*(\delta)^2$ multiplication operations. It follows that the costs associated with solving the linear problem are overwhelmed by the costs associated with the evaluations of the derivatives of the Hamiltonian (14) in (1), which (as argued below) requires at least $M_*(\delta)^2$ evaluations of the derivatives of the free space Green’s function. Hence the additional costs of solving the linear system (9) can be safely neglected.

Comparing the costs of evaluating the derivatives of an image model Hamiltonian (Eq. (2), with $G(\mathbf{x}, \mathbf{x}')$ given by e.g. (20) below) to the VOR-MFS Hamiltonian (14), the former requires $4N^2$ evaluations of the derivatives of G_0 and the latter $(N + M_*(\delta) + \bar{P})^2$ evaluations, where $\bar{P} < N$ is the average number of pseudo-images in use. For $N \gg M_*(\delta)$ VOR-MFS therefore becomes *cheaper* than the corresponding image model (since \bar{P} is roughly proportional to N). VOR-MFS is therefore very well-suited to large N super-computer simulations of the type performed by Yatsuyanagi et al. [42]. Note that there is evidently an optimization problem, which has not yet been explored in detail, concerning how to best choose the pseudo-image protocol to minimize $M_*(\delta) + \bar{P}$ in VOR-MFS.

The costs associated with decreasing the tolerance parameter δ are primarily associated with the underlying adaptive time-stepping scheme described above in Section 2.1. For the present fourth-order (RK4) scheme, a decrease in δ by a factor of sixteen results in a doubling of the number of substeps ($m_* \rightarrow m_* + 1$) needed over each integration interval Δt . In VOR-MFS there is an addition cost associated with an increase in the number of MFS points $M_*(\delta)$, but because this increase is logarithmic in δ the additional cost is relatively small, particularly if N is large.

A further cost for VOR-MFS, which applies when the system being integrated is no longer the 2D Euler system, is the additional cost of evaluating e.g. modified Bessel functions (see Eq. (5)), when calculating the gradients of H . This cost can be considerable, and the use of fast Bessel function routines is recommended.

3. Test cases for VOR-MFS

3.1. Test case I: multiple 2D Euler vortices in a circular domain

The first test for VOR-MFS will consider the dynamics of N 2D Euler vortices in a unit circle domain. The performance of VOR-MFS will be tested against an exact ‘image’ model to be described.

The exact Hamiltonian H for the motion of N 2D Euler vortices in a unit circle is given by (2) with

$$G(\mathbf{x}, \mathbf{x}') = \frac{1}{2\pi} \log |\mathbf{x} - \mathbf{x}'| - \frac{1}{4\pi} \log \left(1 - 2\mathbf{x} \cdot \mathbf{x}' + |\mathbf{x}|^2 |\mathbf{x}'|^2 \right), \tag{20}$$

where the first term can be recognized to be $G_0(\mathbf{x}, \mathbf{x}')$ and the second is therefore $g(\mathbf{x}, \mathbf{x}')$. Viewed as a function of \mathbf{x} , (20) is equivalent (up to a dynamically irrelevant function of \mathbf{x}') to the streamfunction induced in an unbounded domain by a vortex of circulation $+1$ at \mathbf{x}' plus a vortex of circulation -1 at the image location $\mathbf{x}^* = \mathbf{x}'/|\mathbf{x}'|^2$. The exact expression for $G(\mathbf{x}, \mathbf{x}')$ allows (1) to be solved directly using the adaptive time-stepping routine described in Section 2.1. We refer to this model henceforth as the image model.

Two tests used to assess VOR-MFS are conservation of the Hamiltonian H and of angular momentum

$$L = \frac{1}{2\pi} \sum_{i=1}^N \Gamma_i |\mathbf{x}_i|^2. \tag{21}$$

Conservation of L follows from the rotational symmetry of the unit circle domain. The relative error measures

$$\delta_H(t) = \left| \frac{H(t) - H(0)}{H_r} \right|, \quad \delta_L(t) = \left| \frac{L(t) - L(0)}{L_r} \right| \tag{22}$$

are adopted as the principal means of evaluation of VOR-MFS accuracy. Here H_r and L_r are reference magnitudes for the Hamiltonian and angular momentum, chosen to be their mean and standard deviation respectively, as calculated from 100 samples based on uniformly distributed vortex positions. Recall that VOR-MFS uses convergence of mean vortex position as its criterion for advancement (see Eq. (6)), hence conservation of H and L are not targetted directly. Numerical control over the error measures δ_H and δ_L is therefore an important internal consistency check for the algorithm.

To compare results between the image model and VOR-MFS, the equations of motion (1) are integrated for 100 non-dimensional time units with $N = 4$ vortices (with circulations $\Gamma_i = +1, +1, -1, -1$), using each model. The motion of four vortices in a bounded domain is known to be chaotic in general [32] and consequently provides a robust test. Results for three different values of the tolerance δ are compared ($\delta = 10^{-6}, 10^{-8}, 10^{-10}$) with the integration interval set to be

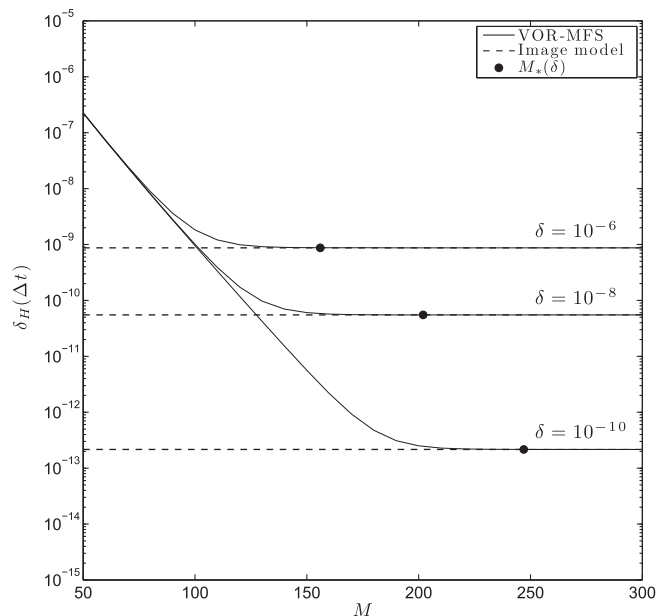


Fig. 3. Dependence of relative numerical error $\delta_H(\Delta t)$ in the Hamiltonian H , at the end of a single integration interval Δt , upon the number of MFS charge points M used by VOR-MFS (solid curves). The largest errors over 100 realizations of uniformly distributed random initial conditions are shown and results are given for several values of the adaptive time-stepping tolerance ($\delta = 10^{-6}, 10^{-8}, 10^{-10}$). Dashed lines show the corresponding error in the image model. The values $M = M_*(\delta)$ obtained from Eq. (19) are illustrated as solid points on each curve.

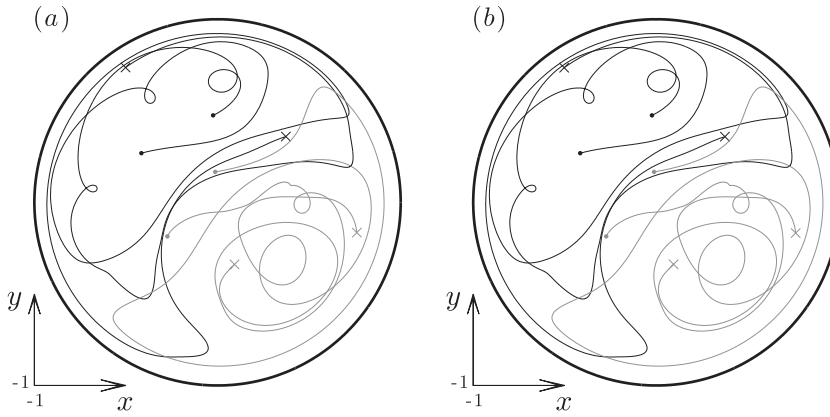


Fig. 4. (a) Vortex trajectories as calculated using the image model over 20 nondimensional time units with tolerance parameter $\delta = 10^{-8}$. Black curves show positive vortices and grey curves negative vortices. Initial positions are plotted as filled circles and final positions as crosses. (b) As (a) but for VOR-MFS with $M_*(\delta) = 202$.

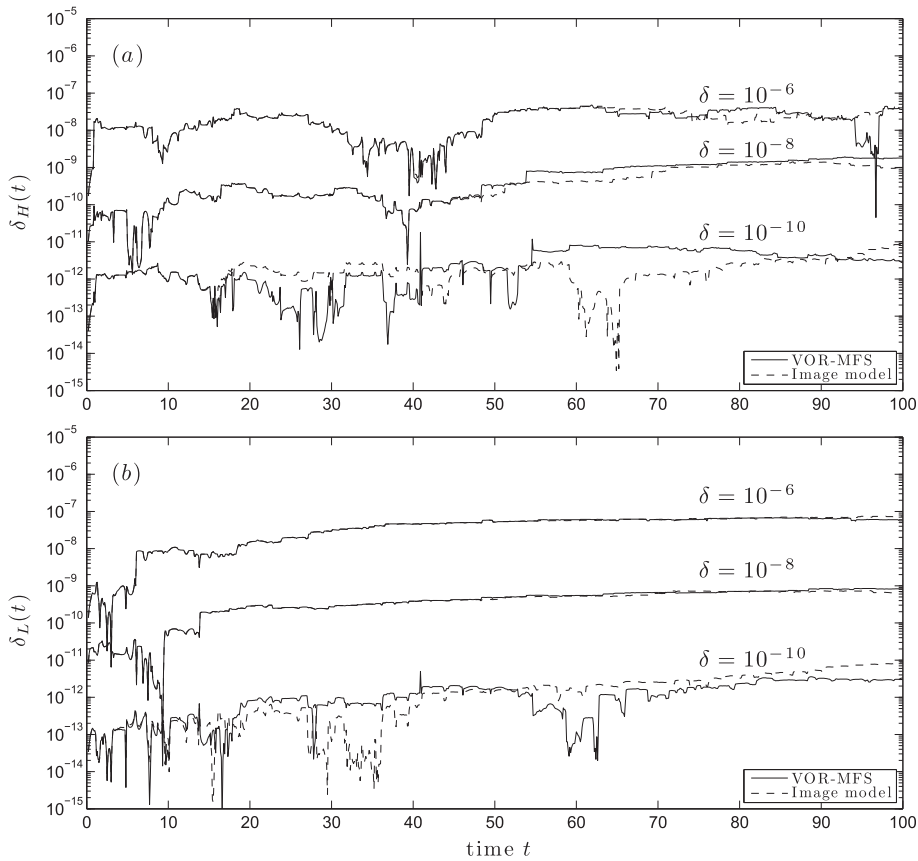


Fig. 5. Time evolution of the error measures (a) $\delta_H(t)$ (Hamiltonian error) and (b) $\delta_L(t)$ (angular momentum error) during VOR-MFS model integrations (solid curves) and the image model integrations (dashed curves). Three values of the tolerance parameter $\delta = 10^{-6}, 10^{-8}, 10^{-10}$ are shown with $M = M_*(\delta) = 156, 202, 248$ the respective number of MFS charge points.

$\Delta t = 0.1$. For VOR-MFS, the MFS charge points are located at $R = 1.1$, and the procedure detailed in Section 2.4 is followed to set the number of MFS charge points to be $M = M_*(\delta) = 156, 202, 248$ respectively. Pseudo-images are introduced smoothly for radii greater than $R_1 = 0.8$ and with $R_2 = 0.9$ (see Eq. 13) at positions $\mathbf{x}_j^* = \mathbf{x}_j/|\mathbf{x}_j|^2$.

To confirm that the number of MFS points $M = M_*(\delta)$ is adequate in each case, Fig. 3 shows $\delta_H(\Delta t)$ ($H_r = -0.366$, 3 sig. fig.) as a function of M for VOR-MFS (solid curves), and the corresponding error in the image model (dashed lines). The results are

taken from the worst case of 100 short integrations (length $\Delta t = 0.1$) with uniformly distributed random initial vortex placements as initial conditions. Fig. 3 confirms that the method of Section 2.4 is broadly successful in selecting the minimum value $M = M_*(\delta)$ for which errors due to MFS are significantly less than errors due to the adaptive time-stepping scheme (dashed curves).

Fig. 4 illustrates vortex trajectories calculated using both the image model and VOR-MFS over 20 nondimensional time units. Numerical parameters are $\delta = 10^{-8}$ and $M_*(\delta) = 202$, as in the middle case above. The same initial conditions are used in each case and it is clear from the figure that VOR-MFS accurately reproduces the image model trajectories during a period in which the vortices make multiple circuits of the domain. The mean difference in vortex positions between the two runs at $t = 20$ is 1.3×10^{-4} . Due to the chaotic nature of the vortex evolution the mean difference grows exponentially and is 6.7×10^{-1} at $t = 40$. Beyond this time the two integrations diverge completely. Note that vortices are within the full pseudo-image region $|\mathbf{x}_j| > R_2 = 0.9$ (see Eq. (13)) for just 7% of the integration.

Fig. 5 shows the time evolution of $\delta_H(t)$ and $\delta_L(t)$ ($L_r = 0.593$, 3 sig. fig.) over the full duration of the VOR-MFS model integrations (solid curves, with $M = M_*(\delta)$ in each case) and image model integrations (dashed curves), where again $\delta = 10^{-6}, 10^{-8}, 10^{-10}$ and $M = M_*(\delta) = 156, 202, 248$. It is evident that in both models $\delta_H(t)$ and $\delta_L(t)$ are controlled (linearly) by the tolerance parameter δ . Fig. 5 demonstrates that the growth of numerical errors in both H and L is comparable in each model.

3.2. Test case II: multiple 2D Euler vortices in a Neumann oval

A more challenging test for VOR-MFS is to simulate point vortex dynamics in a domain with less symmetry than the unit circle. Next VOR-MFS is therefore validated against an image model for 2D Euler dynamics in a domain bounded by a Neumann oval [28]. Neumann ovals, constrained here to have equal area (π), are a one-parameter family of curves defined by the conformal map from the unit circle

$$z = F(Z) = \frac{aZ}{1 - q^2 Z^2}, \quad a = a_\pi(q) = \frac{1 - q^4}{(1 + q^4)^{1/2}}. \tag{23}$$

Here the usual correspondence between the complex plane \mathbb{C} and \mathbb{R}^2 is assumed, i.e. $z = x + iy$ is identified with coordinates $\mathbf{x} = (xy)^T$ in the Neumann oval domain and $Z = X + iY$ with coordinates $\mathbf{X} = (XY)^T$ in the unit circle image domain. The parameter q ($0 \leq q < 1$) controls the shape of the Neumann oval. Here $q = 0.7$ is chosen ($q = 0$ maps the circle to itself).

An image model is available for any conformally mapped domain following application of the Routh rule [32]. Defining $\mathbf{X} = \mathbf{f}(\mathbf{x})$ to be the \mathbb{R}^2 expression of the inverse map of (23), $Z = f(z)$, the Green's function in \mathcal{D} is simply

$$G(\mathbf{x}, \mathbf{x}') = G_c(\mathbf{f}(\mathbf{x}), \mathbf{f}(\mathbf{x}')), \tag{24}$$

where G_c denotes the unit circle Green's function given in (20). The image model is defined by (2) with Green's function (24). Notice that careful evaluation of terms of the form $g(\mathbf{x}, \mathbf{x})$ appearing in (2) is necessary, the important result being [32]

$$g(\mathbf{x}, \mathbf{x}) = g_c(\mathbf{f}(\mathbf{x}), \mathbf{f}(\mathbf{x}')) + \frac{1}{2\pi} \log |f'(z)|,$$

where g_c is the residual Green's function in the unit circle (see Eq. (20)). A numerical image model designed to solve (1) for the specific mapping defined by (23) has been implemented using the adaptive method of Section 2.1. The numerical image model was validated by verifying conservation of H (see below).

The VOR-MFS model is designed as follows. According to [1], MFS charge points in conformal domains are optimally placed when they do not enclose singularities of the Schwarz function associated with $\partial\mathcal{D}$. The Schwarz function $\bar{z} = S(z)$ is a complex form of the equation determining $\partial\mathcal{D}$, i.e. if $h(x, y) = 0$ defines $\partial\mathcal{D}$ in \mathbb{R}^2 , then $\bar{z} = S(z)$ follows from resolving the equation $h((z + \bar{z})/2, (z - \bar{z})/2i) = 0$ in favor of \bar{z} . It is assumed here that $S(z)$ is analytic in the neighborhood of $\partial\mathcal{D}$. For the particular case of (23) it can be shown that $S(z)$ has singularities at

$$z_\pm = \pm i \frac{a_\pi(q)^2 q(1 + q^2)}{2(1 - q^4)^2}, \tag{25}$$

which lie on the image axis outside $\partial\mathcal{D}$. Taking these locations into account, a suitable curve for the charge points, illustrated in Fig. 6, was found to be the Neumann oval with parameters $q = 0.73$ and $a = (1.3)^{1/2} a_\pi(q)$. The spacing of the MFS charge points on this curve follows the 'constant conformal radius' method [1], i.e. the M charge points are equally spaced on the unit circle and then mapped to their Neumann oval by (23). Fig. 6 shows that charge points are concentrated near the regions of maximum curvature of $\partial\mathcal{D}$. Calculations of $M = M_*(\delta)$ following the method of Section 2.4 reveal that a significantly greater number of charge points (approximately twice as many for the same δ) are required for the oval as compared to the circle.

Pseudo-images are introduced much as for the unit circle. First define inner and outer Neumann ovals by (23) with $q_1 = 0.86$ and $a_1 = (0.6)^{1/2} a_\pi(q_1)$ and $q_2 = 0.78$ and $a_2 = (0.76)^{1/2} a_\pi(q_2)$ respectively. Denoting the polar equations of the inner and outer ovals by $r = R_1(\theta)$ and $r = R_2(\theta)$ respectively, the pseudo-image formula (c.f. Eq. (13)) used is

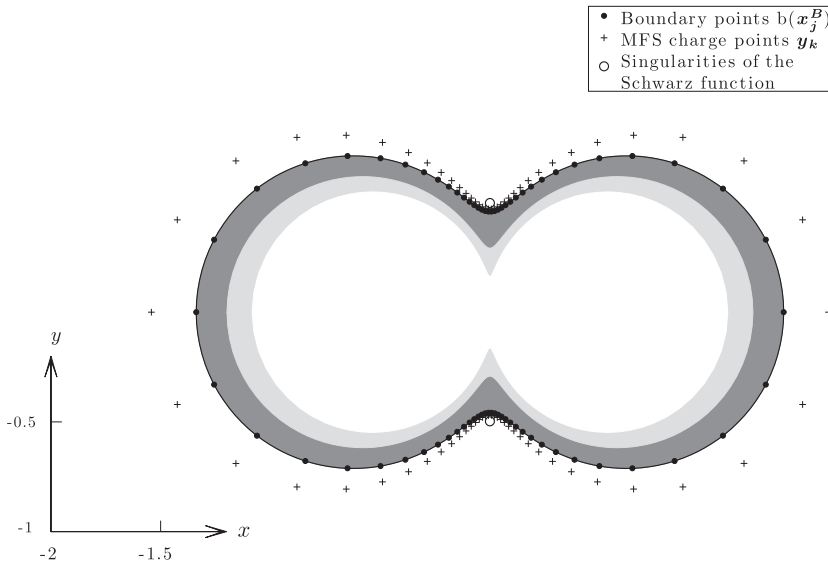


Fig. 6. Geometry of VOR-MFS for the Neumann oval integrations with 70 MFS charge points illustrated. Partial pseudo-images are used in the light grey region and full pseudo-images in the dark grey region. Unfilled circles show the singularities z_{\pm} of the Schwarz function given by (25).

$$\hat{\Gamma}_j = -\Gamma_j = \begin{cases} 1, & |\mathbf{x}_j| \geq R_2(\theta_j), \\ \left(\frac{|\mathbf{x}_j| - R_1(\theta_j)}{R_2(\theta_j) - R_1(\theta_j)} \right)^2, & R_1(\theta_j) \leq |\mathbf{x}_j| < R_2(\theta_j), \\ 0, & |\mathbf{x}_j| < R_1(\theta_j), \end{cases} \quad (26)$$

where $\theta_j = \tan^{-1}(y_j/x_j)$. Pseudo-images are placed at the exact image point in the unit circle image domain and mapped back to the Neumann oval. That is, if a vortex at \mathbf{x}_j maps to \mathbf{X}_j in the image domain then the pseudo-image is placed at $\mathbf{x}_j^* = \mathbf{f}(\mathbf{X}_j/|\mathbf{X}_j|^2)$.

Fig. 7 shows the time evolution of the error measure $\delta_H(t)$ (calculated using H_M) during separate integrations with $N = 4, N = 8$ and $N = 16$ vortices and $H_r = -0.441, -0.895$ and -1.70 to 3 sig. fig. respectively. Equal numbers of positive and negative vortices are used in each case with circulations $\Gamma_i = \pm 1$. The numerical parameters used are integration interval $\Delta t = 0.1$, tolerance $\delta = 10^{-8}$ and number of MFS charge points $M_*(\delta) = 348$. Good conservation properties are evident for all three integrations.

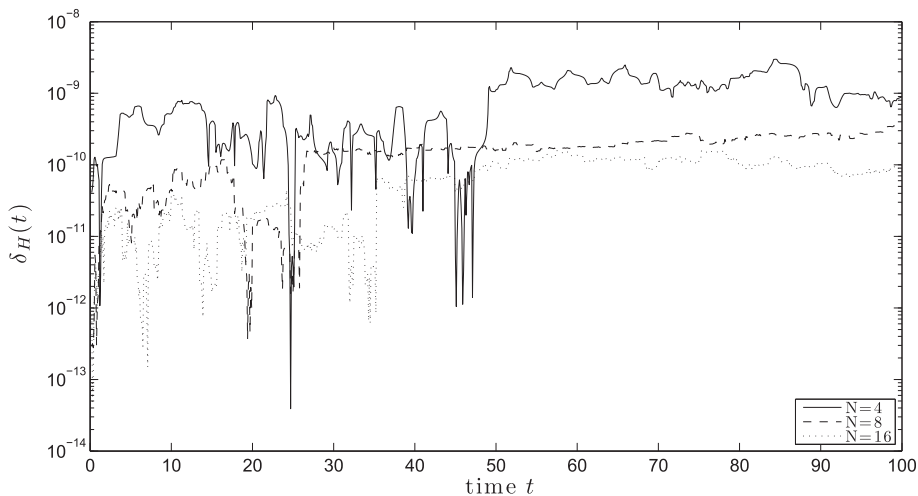


Fig. 7. Time evolution of error measure $\delta_H(t)$ for VOR-MFS integrations of $N = 4, 8$ and 16 2D Euler vortices (solid, dashed and dotted curves respectively.) The value of the tolerance parameter was $\delta = 10^{-8}$ with $M = M_*(\delta) = 348$.

3.3. Test case III: a solitary QGSW vortex in a Neumann oval

Arguably the main strength of VOR-MFS is its capacity to simulate point vortex dynamics in systems other than the 2D Euler equations. One example of such a system is the quasi-geostrophic shallow water (QGSW) model discussed in the introduction, see (5) for its free space Green’s function. Next VOR-MFS will be used to simulate the motion of a single QGSW vortex in the Neumann oval.

Motion of a single vortex governed by (1) is well-known to be confined to isolines of the Hamiltonian H [32], which in the case of a single vortex in a domain \mathcal{D} is given by

$$H(\mathbf{x}_1) = -\frac{1}{2} \Gamma_1^2 g(\mathbf{x}_1, \mathbf{x}_1),$$

where $g(\mathbf{x}, \mathbf{x}')$ is the residual Green’s function for \mathcal{D} . The Hamiltonian H can be approximated at any point \mathbf{x}_1 using MFS (by H_M , see Eq. (14)). An MFS estimate of the isolines of H can therefore be obtained by evaluating H_M on a grid over \mathcal{D} , and contouring the resulting function of \mathbf{x}_1 .

The isolines of H for a QGSW vortex with Rossby radius $\lambda^{-1} = 1$ and circulation $\Gamma_1 = +1$, calculated using the above method with $M = 374$ charge points, is shown in Fig. 8(a). The isolines can be contrasted with those for a 2D Euler vortex shown in Fig. 8(b). The main difference between the two systems is that the (boundary-induced) velocity field experienced by the vortex is much weaker in the QGSW system towards the center of the domain. (Recall from (1) that $\mathbf{u}_1 = \Gamma_1^{-1} \mathbf{k} \times \nabla_{\mathbf{x}_1} H$ and therefore vortex velocities are proportional to the gradient of H .) The weaker velocities can be explained by the fact that the dynamical influence of the QGSW vortex decays exponentially at distances $\gtrsim \lambda^{-1}$, due to the modified Bessel dependence in (5). A QGSW vortex placed a distance $\gg \lambda^{-1}$ from a domain boundary therefore moves as if the boundary is absent.

The thick dashed lines on Fig. 8 show dynamical trajectories calculated explicitly using VOR-MFS (for the QGSW vortex) and the image model (for the 2D Euler vortex) for 35 non-dimensional time units. The initial condition is identical for both runs $\mathbf{x}_1(0) = (0.805 \ 0)^T$. However, the behavior is different due to the different dynamics: the QGSW vortex recirculates

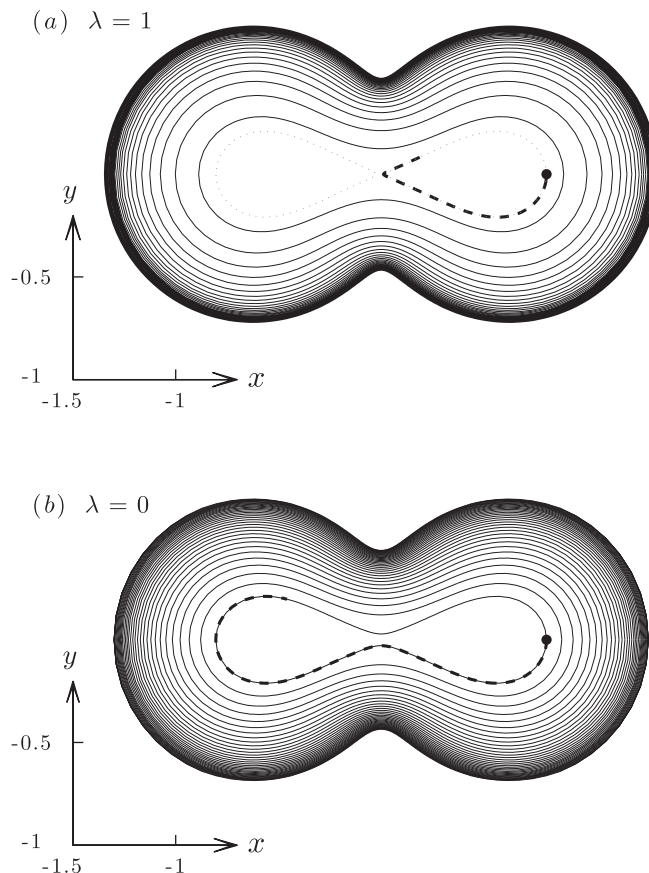


Fig. 8. Isolines of $H(\mathbf{x}_1)$ for (a) a solitary QGSW vortex with $\lambda^{-1} = 1$ and $\Gamma_1 = 1$ (calculated as H_M with $M = 374$), and (b) a solitary 2D Euler vortex, in the Neumann oval given by (23) with $q = 0.7$. The thick dashed lines in each panel show the dynamically calculated trajectory of a vortex with initial position $\mathbf{x}_1(0) = (0.805 \ 0)^T$ over 35 time units, with $\delta = 10^{-8}$. The contour interval is 0.078 in both panels except for the grey dotted contour in (a) (at level 0.097) plotted to illustrate the predicted trajectory.

within the same lobe, whereas the 2D Euler vortex circulates between the two lobes. It is also clear that, as expected, the 2D Euler vortex travels considerably further during the same time period.

Fig. 9 shows the time evolution of $\delta_H(t)$ ($H_r = 0.216$, 3 sig. fig.) during a further QGSW integration with $\mathbf{x}_1(0) = (0 \ 0.3)^T$, over 100 non-dimensional time units, or approximately four complete circuits of the domain. Results are shown for three different values of the tolerance parameter $\delta = 10^{-6}, 10^{-8}$ and 10^{-10} , with corresponding numbers of MFS charge points $M_*(\delta) = 290, 374, 460$. The Hamiltonian error measure $\delta_H(t)$ is evidently linearly controlled by the tolerance parameter δ .

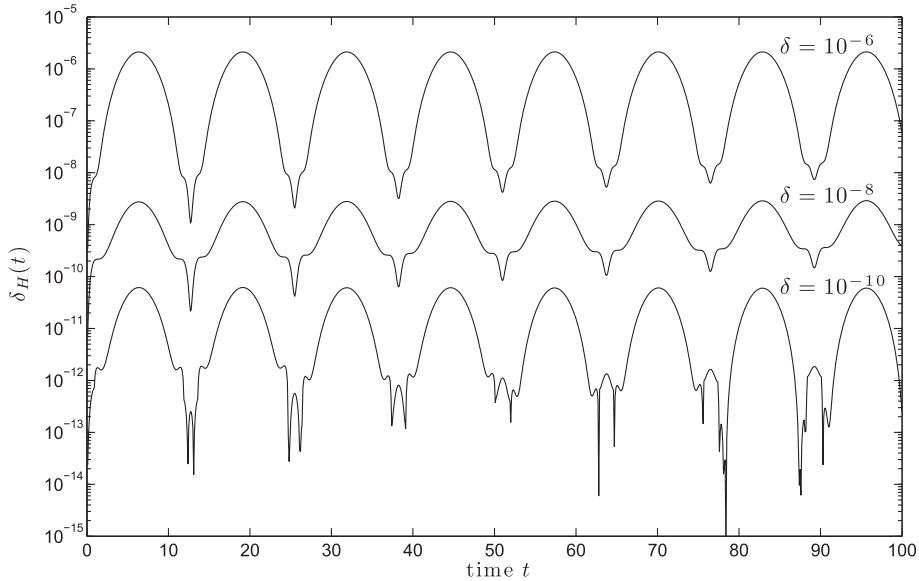


Fig. 9. Time evolution of the error measure $\delta_H(t)$ (where H is estimated by H_M) over 100 non-dimensional time units (corresponding to approximately four complete circuits of the domain) for an QGSW vortex with $\lambda = 1$. Three values of the tolerance parameter $\delta = 10^{-6}, 10^{-8}, 10^{-10}$ are shown with $M = M_*(\delta) = 290, 374, 460$ the respective number of MFS charge points.

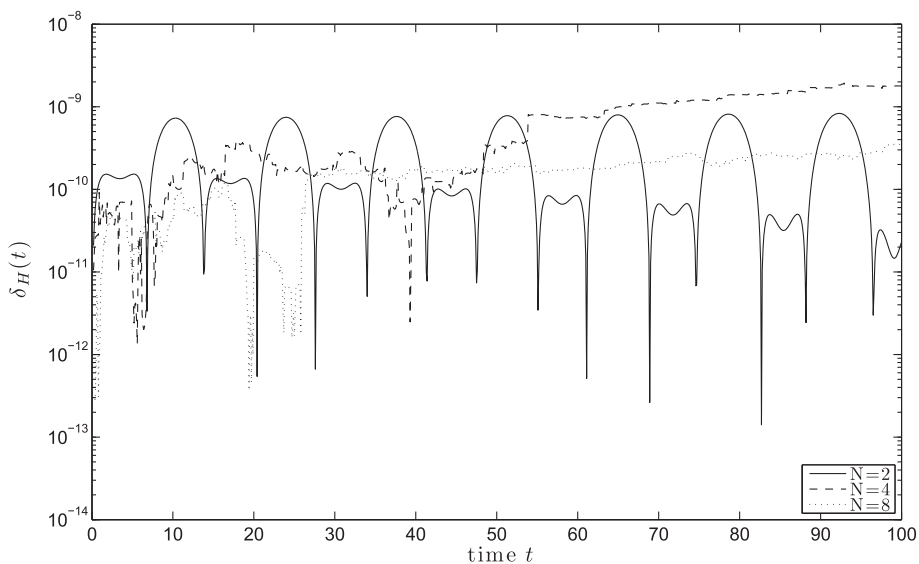


Fig. 10. Time evolution of error measure $\delta_H(t)$ (where H is estimated by H_M) for VOR-MFS integrations with $N = 2, 4$ and 8 QGSW vortices (solid, dashed and dotted curves respectively). The value of the tolerance parameter was $\delta = 10^{-8}$ with $M = M_*(\delta) = 348$.

3.4. Test case IV: multiple QGSW vortices in a Neumann oval

A final test for VOR-MFS is the simulation of the dynamics of many QGSW vortices in a Neumann oval. The dynamics of two or more vortices are chaotic and therefore more challenging numerically. As above, the main means of validating the algorithm is by verifying conservation of H (calculated as H_M from Eq. (14)).

Fig. 10 shows the evolution of the error measure $\delta_H(t)$ for the Hamiltonian for three different runs with $N = 2, 4$ and 8 vortices and $H_r = -0.366, -0.719$ and -1.16 , to 3 sig. fig. respectively. Numerical parameters are as for the 2D Euler calculations described in Section 3.2. As in the 2D Euler case good convergence properties are evident.

4. Conclusions

A new algorithm VOR-MFS has been presented above. It is designed to solve generalized point vortex models in arbitrary two-dimensional domains. The main advantages of the new algorithm are:

1. VOR-MFS requires knowledge of only the free-space (\mathbb{R}^2) Green's function $G_0(\mathbf{x}, \mathbf{x}')$ of the point vortex model in question, as opposed to the domain-adapted Green's function (required e.g. by image-based models). VOR-MFS can therefore be used to investigate the alternative point vortex models of geophysical interest discussed in the introduction (QGSW, SQG, etc.). Additionally, VOR-MFS can be used to solve the 2D Euler system in domains for which the Green's function $G(\mathbf{x}, \mathbf{x}')$ is not known explicitly or is expensive to calculate.
2. Subject to certain caveats [1], the MFS algorithm converges exponentially with the number of charge points M . Hence it is practical to choose M in order that the error associated with using the VOR-MFS algorithm is comparable to that of the underlying adaptive time-stepping scheme (see Section 2.4).
3. The number M of MFS charge points required converges as the number of vortices $N \rightarrow \infty$. Consequently, for sufficiently large N , VOR-MFS becomes no more expensive to integrate than an image model adapted to the same problem.

One difficulty for the MFS method occurs when parts of the domain \mathcal{D} are very thin (e.g. a flat plate or protrusion). In such domains VOR-MFS is likely to perform more like a boundary-integral method, similar to that in [33]. A further caveat, is that complicated domains that require a large number of MFS charge points could result in numerical difficulties, due to limitations associated with the size and apparent conditioning of the linear system (9). As discussed in Section 2.2, this presents minimal practical problems.

The VOR-MFS algorithm opens up a number of interesting pathways for future research. For example, VOR-MFS could be used to test statistical mechanics predictions of the behavior of the geophysical point vortex models mentioned above [11,35]. Chen et al. [4] has demonstrated that MFS is effective in multiply connected domains, hence (for example) VOR-MFS could be used to validate and extend recent results describing vortex trajectories around islands [8]. Another possibility is that, with a few minor adaptations, VOR-MFS could be extended to study the dynamics of point vortex 'hetons' [18], i.e. two-layer quasi-geostrophic vortices of relevance in oceanography [9,24,25]. Further, the dynamics of large ensembles of three-dimensional quasi-geostrophic vortices has also prompted considerable interest [40], including numerical simulations of single-signed point vortices in an unbounded domain [31,37]. There is potential for VOR-MFS to be extended to study the three-dimensional system in bounded domains, permitting the study of 'neutral' systems in which vortices of both signs are present.

Finally, it is interesting to speculate on whether or not the MFS algorithm could be used effectively to implement boundary conditions in dynamical models with piece-wise constant vorticity (contour dynamics, e.g. [10]) or even in models aiming to represent continuous vorticity distributions. In both cases the effective treatment of the continuous analogue of the 'pseudo-images' discussed in Section 2.3 above will be paramount.

Acknowledgement

TLA thanks the Dept. of Mathematics at University College London for providing funding for research through a departmental teaching assistant fellowship.

References

- [1] A.H. Barnett, T. Betcke, Stability and convergence of the method of fundamental solutions for Helmholtz problems on analytic domains, *J. Comput. Phys.* 227 (14) (2008) 7003–7026.
- [2] A. Bogomolny, Fundamental solutions method for elliptic boundary value problems, *SIAM J. Numer. Anal.* 22 (4) (1985) 644–669.
- [3] O. Bühler, Statistical mechanics of strong and weak point vortices in a cylinder, *Phys. Fluids* 14 (7) (2002) 2139–2149.
- [4] K.H. Chen, J.H. Kao, J.T. Chen, D.L. Young, M.C. Lu, Regularized meshless method for multiply-connected-domain Laplace problems, *Eng. Anal. Bound. Elem.* 30 (10) (2006) 882–896.
- [5] I.P. Christiansen, Numerical simulation of hydrodynamics by the method of point vortices, *J. Comput. Phys.* 13 (3) (1973) 363–379.
- [6] P. Constantin, A.J. Majda, E. Tabak, Formation of strong fronts in the 2D quasigeostrophic thermal active scalar, *Nonlinearity* 7 (1994) 1495–1533.
- [7] D.G. Crowdy, J.S. Marshall, Analytical formulae for the Kirchhoff–Routh path function in multiply connected domains, *Proc. R. Soc. Lond. A* 461 (2060) (2005) 2477–2501.
- [8] D.G. Crowdy, J.S. Marshall, The motion of a point vortex around multiple circular islands, *Phys. Fluids* 17 (5) (2005) 056602.

- [9] M.T. DiBattista, A.J. Majda, Equilibrium statistical predictions for baroclinic vortices: the role of angular momentum, *Theor. Comput. Fluid Dyn.* 14 (2001) 293–322.
- [10] D.G. Dritschel, Contour dynamics and contour surgery: numerical algorithms for extended, high-resolution modelling of vortex dynamics in two-dimensional, inviscid, incompressible flows, *Comput. Phys. Rep.* 10 (3) (1989) 77–146.
- [11] S.F. Edwards, J.B. Taylor, Negative temperature states of two-dimensional plasmas and vortex fluids, *Proc. R. Soc. Lond. A* 336 (1606) (1974) 257–271.
- [12] G. Fairweather, A. Karageorghis, The method of fundamental solutions for elliptic boundary value problems, *Adv. Comput. Math.* 9 (1998) 69–95.
- [13] M.A. Golberg, C.S. Chen, *Discrete Projection Methods for Integral Equations*, Computational Mechanics Publications, Southampton, 1996.
- [14] M.A. Golberg, C.S. Chen, The method of fundamental solutions for potential, Helmholtz and diffusion problems, in: M.A. Golberg (Ed.), *Boundary Integral Methods – Numerical and Mathematical Aspects*, Computational Mechanics Publications, Boston, 1999, pp. 103–176.
- [15] M.A. Golberg, C.S. Chen, S.R. Karur, Improved multiquadric approximation for partial differential equations, *Eng. Anal. Bound. Elem.* 18 (1) (1996) 9–17.
- [16] L. Greengard, V. Rokhlin, A fast algorithm for particle simulations, *J. Comput. Phys.* 135 (2) (1997) 280–292.
- [17] I.M. Held, R.T. Pierrehumbert, S.T. Garner, K.L. Swanson, Surface quasi-geostrophic dynamics, *J. Fluid Mech.* 282 (1995) 1–20.
- [18] N.G. Hogg, H.M. Stommel, Hetonic explosions: the breakup and spread of warm pools as explained by baroclinic point vortices, *J. Atmos. Sci.* 42 (1985) 1465–1476.
- [19] M.N. Juckes, Quasigeostrophic dynamics of the tropopause, *J. Atmos. Sci.* 51 (1994) 2756–2779.
- [20] M. Katsurada, A mathematical study of the charge simulation method: II, *J. Fac. Sci. Univ. Tokyo Sec. IA Math.* 36 (1) (1989) 135–162.
- [21] M. Katsurada, H. Okamoto, A mathematical study of the charge simulation method: I, *J. Fac. Sci. Univ. Tokyo Sec. IA Math.* 35 (3) (1988) 507–518.
- [22] T. Kitagawa, On the numerical stability of the method of fundamental solution applied to the Dirichlet problem, *Jpn. J. Appl. Math.* 5 (1) (1988) 123–133.
- [23] T. Kitagawa, Asymptotic stability of the fundamental solution method, *J. Comput. Appl. Math.* 38 (1991) 263–269.
- [24] S. Legg, J. Marshall, A Heton model of the spreading phase of open-ocean deep convection, *J. Phys. Oceanogr.* 23 (1993) 1040–1056.
- [25] S. Legg, J. Marshall, The influence of the ambient flow on the spreading of convective water masses, *J. Mar. Res.* 56 (1998) 107–139.
- [26] C.C. Lin, On the motion of vortices in two dimensions: I. Existence of the Kirchhoff–Routh function, *Proc. Natl Acad. Sci.* 27 (1941) 570–575.
- [27] C.C. Lin, On the motion of vortices in two dimensions: II. Some further investigations on the Kirchhoff–Routh function, *Proc. Natl Acad. Sci.* 27 (1941) 575–577.
- [28] E. Lundberg, Laplacian growth, elliptic growth, and singularities of the Schwarz potential, *J. Phys. A: Math. Theor.* 44 (13) (2011) 135202.
- [29] A.J. Majda, A.L. Bertozzi, *Vorticity and Incompressible Flow*, Cambridge Univ. Press, Cambridge, 2001.
- [30] A. Miguel, Adaptive geometric numerical integration for point vortex dynamics, *Phys. Rev. E* 74 (4) (2006) 046706.
- [31] T. Miyazaki, T. Sato, N. Takahashi, Maximum entropy states of quasi-geostrophic point vortices, *Phys. Fluids* 24 (5) (2012) 056601.
- [32] P.K. Newton, *The N-Vortex Problem: Analytical Techniques*, Springer-Verlag, New York, 2001.
- [33] R.S. Nilawar, E.R. Johnson, N.R. McDonald, Finite Rossby radius effects on vortex motion near a gap, *Phys. Fluids* 24 (6) (2012) 066601.
- [34] J. Pedlosky, *Geophysical Fluid Dynamics*, Springer-Verlag, New York, 1987.
- [35] Y.B. Pointin, T.S. Lundgren, Statistical mechanics of two-dimensional vortices in a bounded container, *Phys. Fluids* 19 (10) (1976) 1459–1470.
- [36] D.I. Pullin, P.G. Saffman, Long-time symplectic integration: the example of four-vortex motion, *Proc. R. Soc. Lond. A* 432 (1886) (1991) 481–494.
- [37] S. Hoshi, T. Miyazaki, Statistics of quasi-geostrophic point vortices, *Fluid Dyn. Res.* 40 (9) (2008) 662–678.
- [38] P.G. Saffman, *Vortex Dynamics*, Cambridge Univ. Press, Cambridge, 1992.
- [39] Y.S. Smyrlis, A. Karageorghis, Efficient implementation of the MFS: the three scenarios, *J. Comput. Appl. Math.* 227 (1) (2009) 83–92.
- [40] J. von Hardenberg, J.C. McWilliams, A. Provenzale, A. Shchepetkin, J.B. Weiss, Vortex merging in quasi-geostrophic flows, *J. Fluid Mech.* 412 (1606) (2000) 331–353.
- [41] C.T. Wu, F.L. Yang, D.L. Young, Application of the method of fundamental solutions and the generalized Lagally theorem to the interaction of solid body and external singularities in an inviscid fluid, *CMC – Comput. Mat. Contin.* 23 (2) (2011) 135–153.
- [42] Y. Yatsuyanagi, Y. Kiwamoto, H. Tomita, M.M. Sano, T. Yoshida, T. Ebisuzaki, Dynamics of two-sign point vortices in positive and negative temperature states, *Phys. Rev. Lett.* 94 (2005) 054502.
- [43] M.Q. Zhang, M.Z. Qin, Explicit symplectic schemes to solve vortex systems, *Comput. Math. Appl.* 26 (5) (1993) 51–56.